The Astrophysical Journal, 723:1651–1664, 2010 November 10 doi:10.1088/0004-637X/723/2/1651


# EVIDENCE OF SOLAR FLARE TRIGGERING DUE TO LOOP–LOOP INTERACTION CAUSED BY FOOTPOINT SHEAR MOTION

Pankaj Kumar[1], A. K. Srivastava[1,4], B. V. Somov[2], P. K. Manoharan[3], R. Erdélyi[4], and Wahab Uddin[1]
[1] Aryabhatta Research Institute of Observational Sciences (ARIES), Nainital-263129, India; pkumar@aries.res.in, aks@aries.res.in
[2] Astronomical Institute, Moscow State University, Universitetskij Prospekt 13, Moscow 119992, Russia
[3] Radio Astronomy Centre, NCRA, Tata Institute of Fundamental Research, Udhagamandalam (Ooty) 643 001, India
[4] Solar Physics and Space Plasma Research Centre (SP$^2$RC), Department of Applied Mathematics, The University of Sheffield, Sheffield S3 7RH, UK
*Received 2010 June 25; accepted 2010 September 6; published 2010 October 26*

## ABSTRACT

We analyze multi-wavelength data of an M7.9/1N class solar flare which occurred on 2006 April 27 in AR NOAA 10875. *GOES* soft X-ray images provide the most likely signature of two interacting loops and their reconnection, which triggers the solar flare. *TRACE* 195 Å images also reveal the loop–loop interaction and the formation of "X" points with converging motion ($\sim$30 km s$^{-1}$) at the reconnection site in between this interacting loop system. This provides evidence of progressive reconnection and flare maximization at the interaction site in the active region. The absence of type III radio bursts during this time period indicates no opening of magnetic field lines during the flare energy release, which implies that the change of field line connectivity/orientation occurred only during the loop–loop interaction and reconnection process. The Ondrejov dynamic radio spectrum shows an intense decimetric (DCIM) radio burst (2.5–4.5 GHz, duration $\sim$3 minutes) during the flare initiation, which reveals the signature of particle acceleration from the reconnection site during loop–loop interaction. The double-peak structures at 4.9 and 8.8 GHz provide the most likely confirmatory signature of the loop–loop interaction at the flare site in the active region. *RHESSI* hard X-ray images also show the loop-top and footpoint sources of the corresponding two-loop system, which act like current-carrying flux tubes with resultant opposite magnetic fields and net force of attraction, and their coalescence during the flare maximum. We also suggest that the shear motion/rotation of the footpoint of the smaller loop, which is anchored in the opposite polarity spot, may be responsible for the flare energy buildup and its eventual release due to the loop–loop interaction.

*Key words:* Sun: chromosphere – Sun: corona – Sun: flares – Sun: magnetic topology – Sun: radio radiation – sunspots

*Online-only material:* color figures

## 1. INTRODUCTION

Solar flares are sudden explosions in the solar atmosphere during which magnetic energy (stored in the twisted and sheared magnetic fields as well as in the current layers between interacting fields) is released in the form of kinetic energy of rapidly moving plasma and, accelerated particles, and thermal energy, heating up the ambient plasma. This primary release of energy takes place in the corona and is accompanied by fast directed ejections (e.g., jets) of plasma, powerful flows of heat, and accelerated particles. They interact with the chromosphere and photosphere, and therefore, create an extremely rich scenario of secondary physical processes observed as solar flares.

It is generally believed and well supported by observations that magnetic reconnection is the key effect that plays a crucial role in annihilating the complex magnetic field structures and the corresponding energy release. Solar flares are mainly distinguished into two categories, i.e., the confined and eruptive flares, which are usually triggered, respectively, in the closed and open morphology of overlying magnetic fields. The instabilities generated in the complex magnetic fields may be one of the most probable causes that drive/trigger the solar flares after the reconnection of unstable flux tubes with the neighborhood field configuration. The emergence of unstable and helical twisted structures can trigger the flares, followed by an eruption (Liu et al. 2008, and references cited there). However, the activation of twisted helical magnetic structures may also play a crucial role in the flare energy buildup and their initiation, with failed eruption depending upon the surrounding magnetic field environment (Kumar et al. 2010; Srivastava et al. 2010 and references cited there).

Solar coronal loops may be considered as current ($\lesssim 10^{12}$ A) carrying conductors. Two current-carrying conductors possess a net attractive force if both have resultant currents in the same direction or resultant magnetic fields in the opposite direction depending upon their orientation with each other. Collisions between current-carrying loops are considered to be the cause of some solar flares (Sakai & de Jager 1996). Based on the loop orientations and size of the interaction region, the current-carrying loop interactions are classified into three categories: (1) one-dimensional coalescence (I type), (2) two-dimensional coalescence (Y type), and (3) three-dimensional coalescence (X type). The theoretical model of Gold & Hoyle (1960) was the first to explain the flare triggering caused by interacting current-carrying loops. However, it is not necessary that the field lines be anti-parallel for two current-carrying conductors to interact. There may be other mechanisms, e.g., footpoint shear motion and rotation, that can also destabilize the loop system, to triggering the flare and eruption. Stronger shear has a greater probability of initiating solar flares and related eruptions (e.g., Tan et al. 2009 and references cited there). *Yohkoh* has also observed some of the flaring events that show three types of loop interaction (I, Y, and X types). In the above-mentioned interactions, the three-dimensional X-type reconnection due to coalescence is the most realistic scenario in the active regions. The necessary condition for three-dimensional X-type interaction is that the length of the interaction region ($L$) should be comparable to the loop diameter ($R$; Sakai & de Jager 1989).

Hanaoka (1996) has found evidence of the emergence of a small loop near one of the footpoints of a pre-existing large coronal loop using observations of various instruments including *Yohkoh*. The interaction of this loop with the larger loop causes flares, microflares, and jets. Liu et al. (1998) have also observed the flare triggered by the I-type interaction of loop systems. Falewicz & Rudawy (1999) have shown the flare energy release caused by two successive X-type interactions of an expanding loop with two high-lying and nearly parallel loop systems. Furthermore, Pohjolainen (2003) has also studied the series of flares from AR 8996 on 2000 May 18–20 and provided evidence of flare triggering due to loop–loop interaction with the observation of moving magnetic features around the sunspot region. Several authors have reported loop–loop interactions as a cause of solar flares. However, further multiwavelength studies are needed to understand the flare-triggering mechanism due to loop–loop interaction and its responses in the various layers of the solar atmosphere. In addition to loop–loop interaction, flare triggering followed by solar eruptions (e.g., coronal mass ejection) can also be caused by the interaction of filament system due to sunspot rotation (e.g., Kumar et al. 2010 and references cited there).

We know that the interacting current loops are not located in the vacuum or the isolating medium, but they lie in the highly conducting plasma penetrated by frozen-in magnetic fields in the solar corona. From the beginning of the evolution of a current-carrying loop system, every change in the current-carrying loop system generates currents in the surrounding plasma and magnetic field. Therefore, we have to take into account the interaction not only between the loops but also the interaction of the loop with these new currents, in particular with the screening current layers between the loops. Moreover, the frozen-in magnetic fields of an active region or an activity complex are typically strong in the corona and have their specific topology determined by the photospheric sources. Henoux & Somov (1987) were the first to show that these effects are essential and must be considered in terms of magnetic reconnection of field-aligned electric currents (see Section 2.4). On the other hand, if there were no current loops related to the twisting of magnetic flux tubes at all even in this case, three-dimensional reconnection between interacting magnetic fluxes gives rise to such a distribution of reconnected magnetic fluxes in the corona that two soft X-ray loops look like they are interacting with each other (Gorbachev & Somov 1989, 1990). That is the reason that observations demonstrating such structures are usually considered to be directly supporting the hypothesis of two interacting currents.

In this paper, we present a multiwavelength study of the M7.9/1N solar flare on 2006 April 27 in AR NOAA 10875, which shows rare observational evidence of the coalescence and the interaction of two current-carrying loops. We report a most likely multiwavelength signature of X-type interaction and coalescence instability in the active region which triggers the solar flare. In Sections 2.1–2.3, we present multiwavelength observations of the event. We discuss our results and conclusions in Sections 2.4, 3, and 4.

## 2. OBSERVATIONS AND DATA

The active region NOAA 10875 was located at S10 E20 on 2006 April 27, showing $\beta\gamma/\beta\gamma\delta$ magnetic configuration, and has produced the M7.9/1N class solar flare. According to the *GOES* soft X-ray flux profile, the flare started at 15:45 UT, was

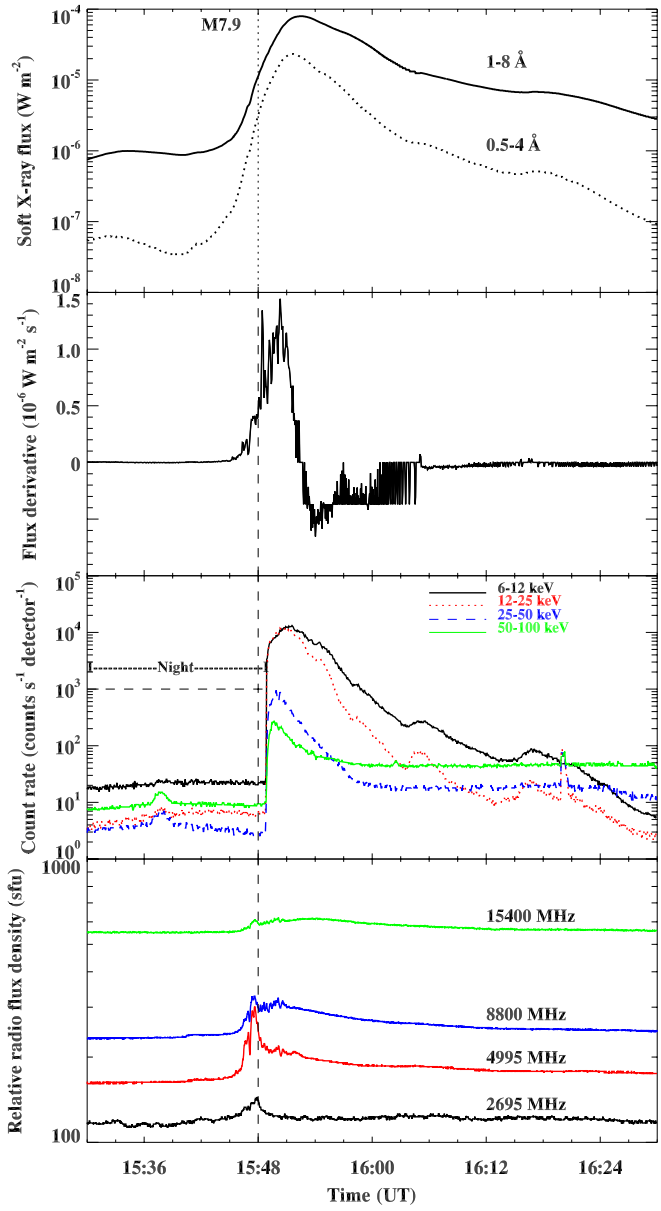


**Figure 1.** Soft X-ray flux, flux derivative, *RHESSI,* and radio flux profiles for the M7.9 flare event on 2006 April 27. The soft X-ray flux derivative matches well with the hard X-ray flux profile. This implies that the accelerated electrons that produce the hard-X-ray also heat the plasma that produces the soft X-ray (Neupert effect). The dotted line in the third panel indicates the *RHESSI* night time.

(A color version of this figure is available in the online journal.)

at its maximum at 15:52 UT, and ended at 15:58 UT. Figure 1 displays the flux profiles in the soft X-ray, soft X-ray derivative, hard X-ray, and radio wavelengths. The flux derivative of soft X-ray matches well with the rise of the hard X-ray flux profile. This implies that the accelerated electrons that produce the hard X-ray also heat the plasma that produces the soft X-ray, obeying the Neupert effect (Neupert 1968). More exactly, this means that the impulsive heating of the solar atmosphere by accelerated electrons can dominate its heating by thermal fluxes from the high-temperature source of flare energy (see Chapter 2 in Somov 1992). So, there is a causal connection between the thermal and nonthermal flare emissions. Further, the radio flux profile exhibits a sharp rise with a double-peak structure mostly in 4.9 and 8.8 GHz at 15:47 UT, which shows

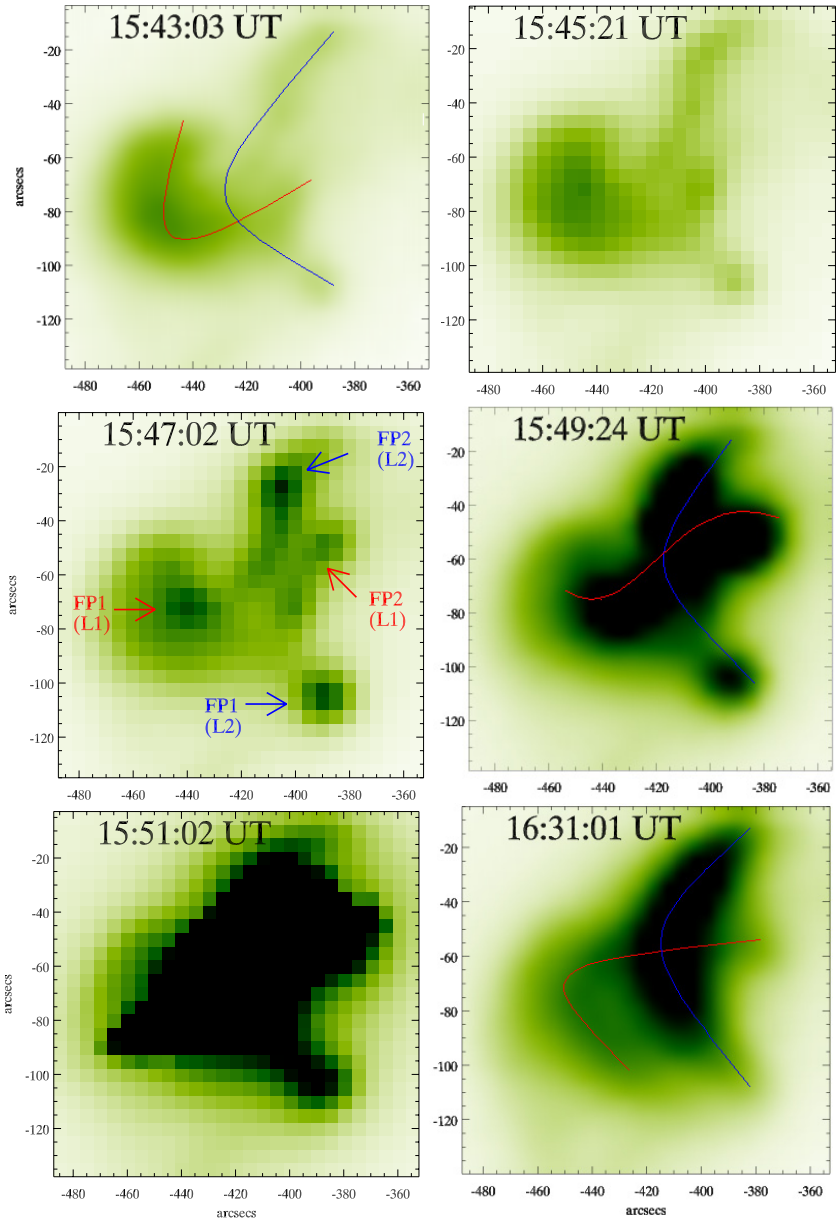


**Figure 2.** *GOES* Soft X-ray coronal negative images (6–60 Å) showing the flare evolution with the interaction of two coronal loops on 2006 April 27. The upper-left panel shows a lower loop system (blue) under a higher loop system (red). The lower loop first looks brighter during flare initiation. The middle-left panel shows the corresponding footpoints of both interacting loops indicated by FP1 (L1) and FP2 (L1) for loop 1 and FP1 (L2) and FP2 (L2) for loop 2, respectively. The bottom-left panels show the flare maximum due to loop–loop interaction and the bottom-right panel indicates the two simplified loops after the flare energy release.

(A color version of this figure is available in the online journal.)

the gyrosynchrotron emission generated by the accelerated electrons at the reconnection (i.e., loop-interaction) site.

### *2.1.* GOES *SXI AND* TRACE *Observations*

We have used *GOES*-SXI observations of the event (Hill et al. 2005; Pizzo et al. 2005). It is a broadband imager in the 6–60 Å bandpass that produces full-disk solar images with ∼1 minute cadence. The images consist of 512 pixels × 512 pixels with 5″ resolution. The FWHM of the telescope point-spread function is ∼10″. A set of selectable thin-film entrance filters allows plasma temperature discrimination, i.e., open, three polyimide (thin, medium, and thick), and three beryllium (thin, medium, and thick). The open and polyimide filters are sensitive to plasma below 2 MK. It is especially suitable for continuous tracking of coronal loops.

Figure 2 displays the selected images of *GOES* SXI before and during the flare activity. Two loop systems have been observed before the flare initiation. One lower loop system (indicated by a red line) lies under a higher loop system (blue). Initially, brightening starts in the lower loop during flare initiation at 15:43 UT. This loop becomes brighter as the flare progresses. The four footpoints of both loop systems become evident at 15:47 UT mainly due to the precipitation of the accelerated electrons from the interaction or the reconnection site. The corresponding footpoints of both interacting loops are indicated by FP1 (L1) and FP2 (L1) for loop 1 and FP1 (L2) and FP2 (L2) for loop 2. As the plasma heats up due to the dissipation of the kinetic energy of the accelerated electrons from the reconnection site, chromospheric evaporation takes place and it fills the interacting loop system in the corona, making these

loops look as if they were crossing each other. The X-type configuration becomes evident at 15:49 UT. The flare maximum takes place at 15:52 UT. After the interaction between the loops, the orientation of the lower loop has changed into a more relaxed state. The solar X-ray imager (SXI) image taken during the decay phase of the flare (at 16:31 UT) clearly shows the orientation change of the lower loop system.

In this figure, the loop shown in red is marked in the upper-left panel as rooted somewhere close to $X \approx -445''$, $Y \approx -50''$. However, in the middle-left panel, the left foot of this loop (marked by FP1(L1) has co-ordinates at $X \approx -440''$, $Y \approx -70''$. Therefore, the shift in the footpoint during the dynamical flare event is $\Delta X = 5''$, $\Delta Y = 20''$. Presumably, this apparent displacement of the footpoint FP1(L1) may be due to the following reasons:

1. A displacement directed out from the photospheric neutral line; therefore, it is related to the motion of the flare ribbons in the opposite directions. Such behavior is typical for the two-ribbon flares.
2. A displacement directed parallel to the photospheric neutral line, which is related to the magnetic shear relaxation.

These two processes can jointly cause the distance between the footpoints to increase or decrease. Investigations in the frame of a more detailed model should be done in order to interpret this feature. It is necessary to compare the kernel displacements observed during the flare with the motions and evolution of magnetic fields in the photosphere before the flares (see Somov et al. 2002).

The *Transition Region and Coronal Explorer* (*TRACE*) provides the opportunity to observe the Sun from chromosphere to corona (Handy et al. 1999). We have used *TRACE* 195 Å (Fe XII, $T \sim 1.5$ MK) and 1600 Å ($T \sim$ 4000–10,000 K). The field of view for each image is 1024 × 1024 with $0''.5$ pixel$^{-1}$ resolution. The typical cadence for *TRACE* images is ∼20–60 s. Figure 3 displays the selected *TRACE* 195 Å images during the flare activity. *TRACE* data have been calibrated and analyzed using standard routines in the solarsoft library.[5] During the flare initiation, brightening was observed along both sides of the photospheric neutral line. Two bright sheared structures are observed at 15:46 UT. The image at 15:48 UT shows the loop–loop interaction and formation of an "X" point in between the interacting loop system. Many interacting small flux threads/tubes may be seen in this image. After the X-type interaction during the impulsive phase of the flare, it seems that the loop threads change their footpoint connectivities. This is the signature of an ongoing reconnection process in the same global configuration of the active region. During 15:42–15:46 UT, the two interacting loops are visible in the soft X-ray *GOES*/SXI images; however, they are not visible in the *TRACE* images during the same time frame. The *GOES*/SXI images represent the high temperature and high coronal part of the loop systems, while the *TRACE* images show the lower part of the loop systems joining the two bright ribbons. In the pre-flare state, the *GOES*/SXI images show that the loop segments are visible due to soft X-ray emission during loop–loop interaction, while at the same time, the plasma at the EUV temperature band is not uploaded in the lower segments of the two loops to make them as visible as the *GOES*/SXI images. However, near the flare maximum and even after the flare, the interacting loop systems are clearly evident in both X-ray and EUV, and imply the presence of plasma at various temperatures, since we see the different segments of the interacting loop systems in *GOES*/SXI and *TRACE* images. Therefore, they look alike albeit with different orientations, as the apex part may be more tilted compared to the lower segments. We can identify the four footpoints of the associated interacting two loop systems. During the interaction, the thickness of the interaction region (indicated by arrows) reduces during the impulsive phase of the flare and it seems that the orientation of the loops is changed during the flare maximum (refer to image at 15:50 UT and onward images). During the sharp impulsive phase, the footpoints of the loop systems do not show significant changes (see the *TRACE* image sequence in Figure 3). This means that the reconnection point, i.e., the loop interaction site, is mostly fixed. The loop-system morphology becomes simple and relaxed during the decay phase of the flare as observed in SXI images (see SXI image at 16:31:01 UT). The thickness of the interaction region is plotted against the *GOES* soft X-ray flux profile (refer to Figure 4). This plot reveals that the X-ray flux rises up as the thickness of the interaction region decreases. This may be the most likely signature of ongoing reconnection at the loop's interaction site. From the linear fit, the typical converging speed is estimated as ∼30 km s$^{-1}$. This speed may be related to the typical inflow speed as observed in other flares (Tsuneta et al. 1997; Yokoyama et al. 2001).

We have overplotted MDI contours over *TRACE* 195 Å images and vice versa (refer to Figure 5). The left footpoints (FP1(L1) and FP2(L2)) of the associated loop systems are anchored in positive polarity field regions whereas the right footpoints (FP1(L2) and FP2(L1)) are anchored in the negative polarity regions.

To investigate the overlying magnetic field environment of this active region, we have used the potential field source surface (PFSS) extrapolation (Altschuler & Newkirk 1969; Schatten et al. 1969) before the flare event at 00:05 UT (see the left panel of Figure 6). The right panel of Figure 6 displays H$\alpha$ images observed at Meudon, which shows flare ribbons during the decay phase (at 16:16 UT) of the flare. It mainly shows four bright kernels, which are the regions where most of the energy flux is concentrated, i.e., the sites of particle precipitation. These are the footpoints of the corresponding reconnecting loop system. These observations support the loop–loop interaction mechanism. For comparison, the location of the flare ribbons' polarities is denoted by "+" (red) and "−" (blue) signs in the *SOHO*/MDI image of the active region (AR10875) with coronal field extrapolation. The coronal magnetic field topology is on average also in agreement with *TRACE* and SXI observations. Figure 7 displays the *TRACE* 1600 Å images during the flare event. Two ribbons, located on both sides of a neutral line, are observed at 15:44 UT. The ribbon on the left shows the sheared "S" shaped structure, whereas the ribbon on the right shows a simple structure.

### 2.2. *Radio and* RHESSI *Observations*

We have used the Ondrejov dynamic radio spectrum data (2–4.5 GHz) during the flare (Jiricka et al. 1993; Jiřička & Karlický 2008). This radiospectrograph uses a 3 m dish and a wide band horn antenna as primary feed. The time resolution is 10 ms and the frequency band is divided into 256 channels, which means that the frequency resolution is about 10 MHz. Figure 8 (upper panel) displays the Ondrejov dynamic radio spectrum on 2006 April 27 showing the intense DCIM radio burst during flare initiation. Moreover, there was no type III burst during this time period (checked against the Wind/WAVES

[5] http://hesperia.gsfc.nasa.gov/ssw/trace/

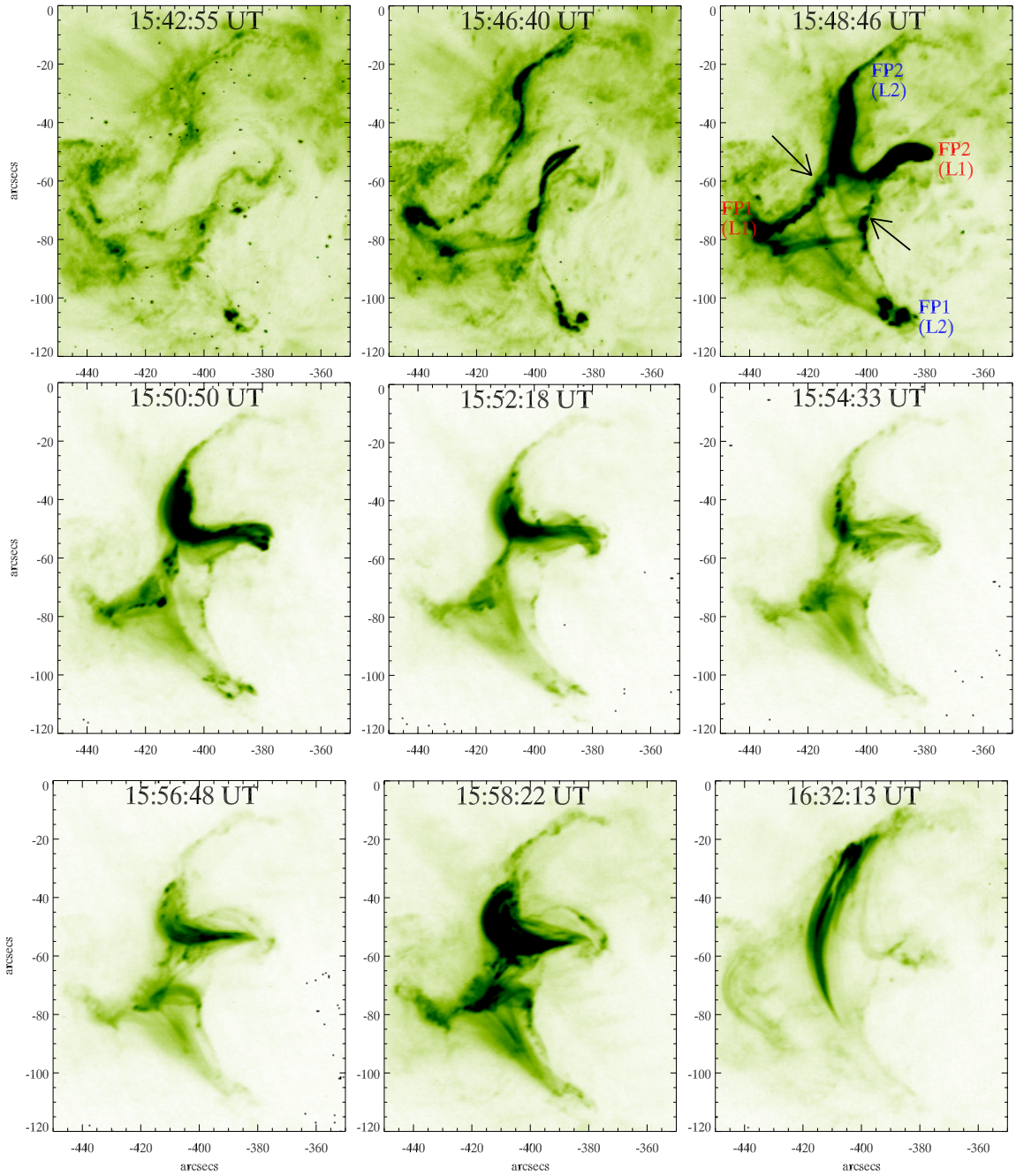


**Figure 3.** *TRACE* 195 Å negative images showing the flare evolution with the interaction of two coronal loops on 2006 April 27. The upper and middle panels show approaching and interacting loops. The flare initiation takes place as the loops approach and maximize at the time of interaction. The corresponding footpoints of the interacting loops are indicated by FP1 (L1) and FP2 (L1) for loop 1 and FP1 (L2) and FP2 (L2) for loop 2. The arrows indicate the interaction region/reconnection site. The bottom right panel shows the relaxation and orientation changes of the loops after interaction.

(A color version of this figure is available in the online journal.)

spectrum). This means that the opening of field lines did not take place during the flare energy release (i.e., during reconnection). The DCIM burst starts with ∼2.5–3 GHz frequency and continues up to 4.5 GHz. This frequency range covers the typical range of heights corresponding to the reconnection site. The burst starts at 15:46 UT and continues up to 15:49 UT for ∼3 minutes. The observed DCIM bursts reveal the signature of particle acceleration from the reconnection site during loop–loop interaction/coalescence.

The US Air Force operates four solar radio observatories at various locations around the world. These are collectively known as the Radio Solar Telescope Network or RSTN. Each observatory monitors solar radio emissions on eight discrete fixed frequencies (245, 410, 610, 1415, 2695, 4995, 8800, and 15,400 MHz) as well as low-frequency spectral emissions in the VHF band. We have used the radio flux data (1 s cadence) from Sagamore Hill. We have selected four radio frequency bands of 2695, 4995, 8800, and 15,000 MHz, which show significant variations in the flux profiles. The radio burst is observed during ∼15:46–15:49 UT (Figure 8, lower panels). The radio flux profiles in 4900 and 8800 MHz show double-peak structures associated with the coalescence of the loop systems. Note that the second double-peak structure is stronger in comparison with the first one, which shows that the superthermal electrons

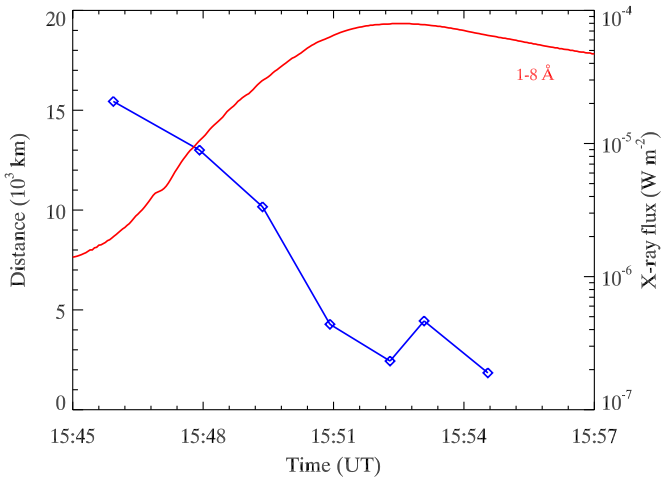


**Figure 4.** Thickness of the interaction region shown by the blue curve (estimated from *TRACE* 195 Å images) plotted against the *GOES* soft X-ray flux profile (red curve). This plot reveals that as the thickness of the interaction region decreases, the soft X-ray flux increases. This may be the most likely signature of ongoing reconnection at the site of loop interaction. The typical converging speed of the interacting region is ∼30 km s$^{-1}$.

(A color version of this figure is available in the online journal.)

generated during the last double peak were accelerated from a higher amount of pre-accelerated electrons (from the preceding coalescence process) than the electrons at the higher beginning of the flare (Karlický & Jiřička 2003). After this burst, we observe the quasi-periodic oscillations specially in the 4995, 8800, and 15,400 MHz frequencies during ∼15:48–15:51 UT for the duration of ∼3 minutes, which may be attributed to modulations by MHD oscillations or nonlinear relaxation oscillations of wave particle interactions. Therefore, MHD waves can modulate the emissions from the trapped electrons (Aschwanden 2004).

The absence of type III radio burst suggests the absence of opening field lines during the reconnection process. Further, we do not observe plasmoid ejection in soft X-ray images from the reconnection site. Therefore, the DCIM radio burst cannot be interpreted as ejected plasmoid from the reconnection site. It should be noted that the burst's starting frequency is ∼2.5–3 GHz, which corresponds to the typical height of post-flare loops and originates in magnetic reconnection regions (i.e., a plasma density of ∼$10^{10}$–$10^{11}$ cm$^{-3}$; Aschwanden 2004). This burst continuation can be seen up to 4.5 GHz in the radio spectrum and higher in single frequency radio flux profiles (i.e., in 2.6, 4.9, 8.8, and 15 GHz). Therefore, we interpret these emissions as being due to nonthermal electrons accelerated from the reconnection site along the soft X-ray loop systems. This may be confirmed by the soft X-ray image at 15:47:02 UT, which shows the four footpoints due to precipitated electrons during the time of radio burst.

The evolution of hard X-ray sources in two selected energy bands (12–25 and 25–50 keV) of the *RHESSI* instrument is shown in Figures 9 and 10. These images have been reconstructed using the PIXON method. In both energy bands, the two separated loop-top sources are visible at 15:49 and 15:50 UT and their coalescence results in a single source (at 15:54 and 15:56 UT). These images also provide the evidence of the two loops' coalescence.

### 2.3. Evolution of the Active Region

Figure 11 displays the selected *TRACE* white light images of the active region on 2006 April 27. FP1 (red) and FP2 (blue) in the top left image show the "+ve" and "–ve" footpoints (indicated by arrows) of the lower loop system, respectively. A careful investigation of the *TRACE* movie reveals the linear/shear motion of a small sunspot of negative polarity (indicated by blue contours) across the neutral line. We have made a

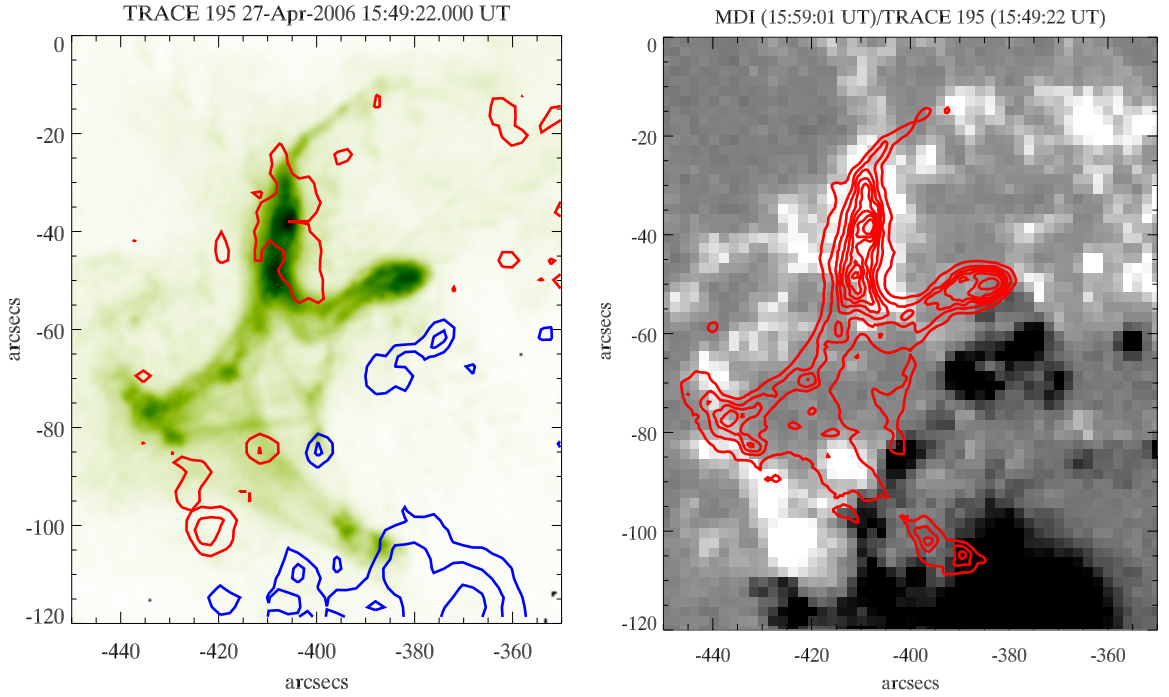


**Figure 5.** Left: MDI contours overlaid on *TRACE* 195 Å images during flare maximum (blue contours indicate the negative whereas red contours show the positive polarity sunspots). The contour levels are ±500, ±1000, ±2000, ±3000 G. Right: *TRACE* 195 Å contours overlaid on the MDI magnetogram (black: negative, white: positive).

(A color version of this figure is available in the online journal.)

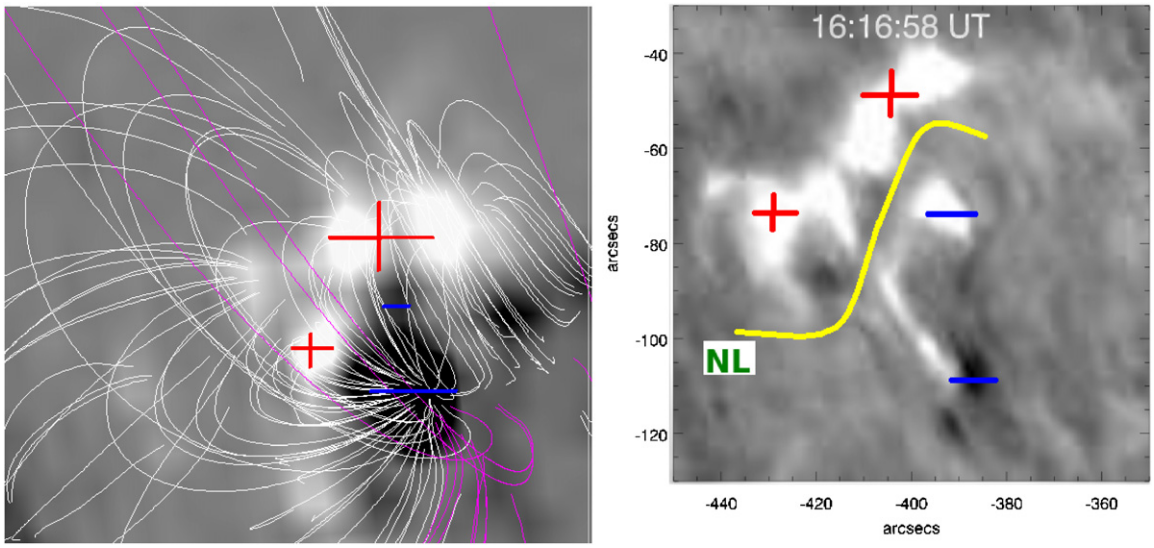


**Figure 6.** Left: potential field source surface (PFSS) extrapolations using the *SOHO*/MDI magnetogram at 00:05:00 UT on 2006 April 27. Right: H$\alpha$ image during the decay phase of the flare showing flare ribbons on both sides of the neutral line (NL), indicated by the yellow line. The polarity at the location of flare ribbons is indicated by "+" and "−" symbols. For comparison, the locations of the flare ribbon polarities are denoted by "+" (red) and "−" (blue) signs in the left panel.

(A color version of this figure is available in the online journal.)

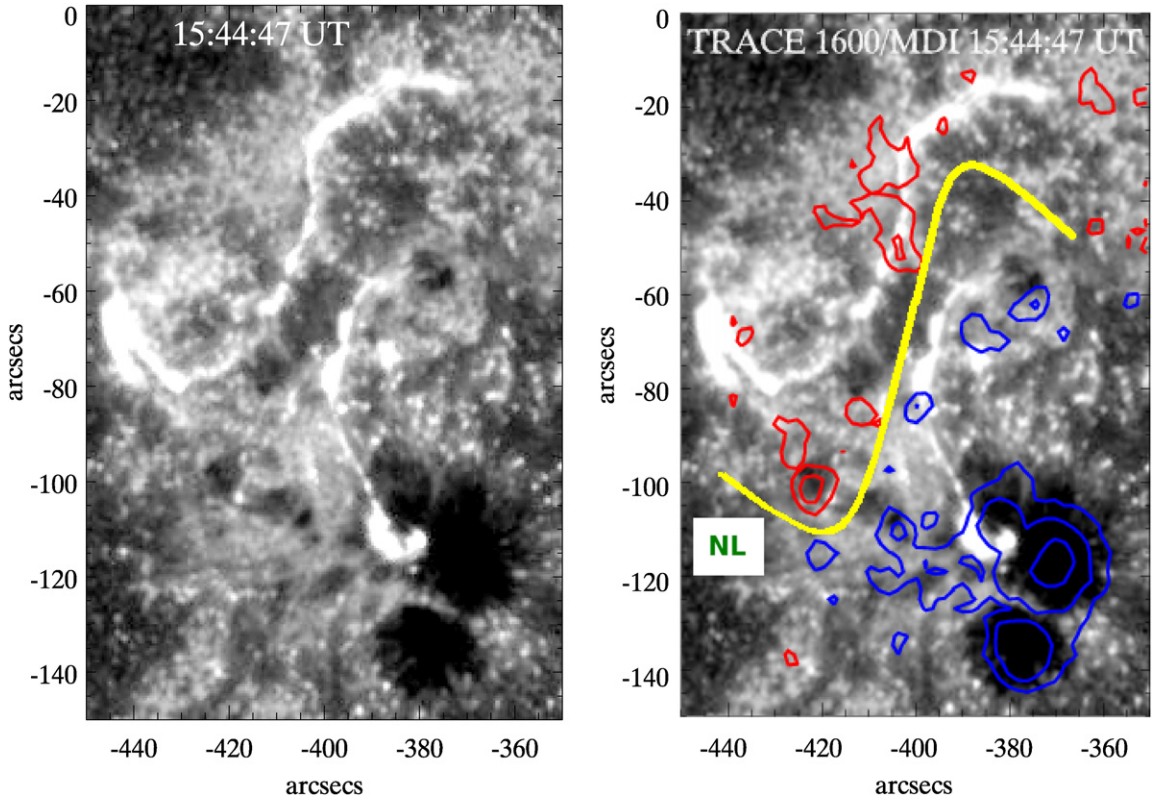


**Figure 7.** Left: *TRACE* 1600 Å images showing the morphology of flare ribbons during the flare. Right: *SOHO*/MDI magnetic field contours overlaid on the *TRACE* 1600 Å image. The red one indicates the positive polarity whereas the blue one shows the negative polarity fields. The contour levels are ±500, ±1000, ±2000, ±3000 G. Ribbons are formed on both sides of the neutral line (NL), drawn in yellow color.

(A color version of this figure is available in the online journal.)

time–distance plot to quantify the linear translational motion of the sunspot. From the linear fit to the data points, the speed of this motion is estimated as ∼0.2 km $s^{-1}$ (662 km $h^{-1}$; see Figure 12). To identify the footpoint of the related loop system anchored in this spot, we overlaid MDI and *TRACE* 195 Å contours over the white-light image (refer to Figure 13, left). This image reveals that one footpoint of the loop system is anchored in this spot. In order to view the photospheric horizontal flow pattern in and around the active region, we use the Fourier Local Correlation Tracking Technique (FLCT) on *SOHO*/MDI images. The FLCT method is described by Fisher & Welsch (2008). The main input parameters for this technique are two images, f1 and f2; the pixel separation scale ($\Delta s$); time separation ($\Delta t$) scale; and a Gaussian window size scale

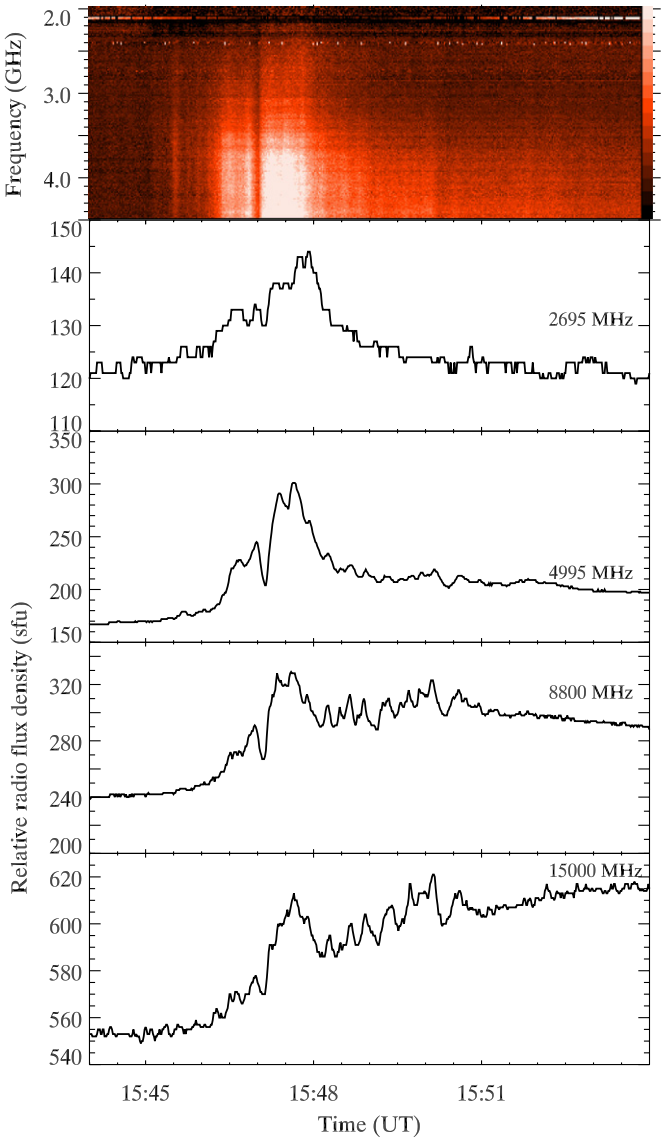


**Figure 8.** Top panel: Ondrejov dynamic radio spectrum on 2006 April 27 showing the intense DCIM radio burst during flare initiation. Additionally, there was no type III burst during this time period (checked against the Wind/WAVES spectrum). That means the opening of field lines did not take place during the flare energy release (i.e., during reconnection). The observed DCIM burst is the signature of particle acceleration from the reconnection site during loop–loop interaction/coalescence. Bottom panel: RSTN 1 s cadence radio flux profiles in 2.6, 4.9, 8.8, and 15 GHz frequencies observed at Sagamore Hill station.

(A color version of this figure is available in the online journal.)

($\sigma$). This routine calculates the velocity (two dimensional) by maximizing the cross-correlation of each image when weighted by the Gaussian window centered on each pixel location. In our study, we use the two *SOHO*/MDI frames at different times before the flare. After a careful investigation, a Gaussian window with a standard deviation of 15″ was chosen. The right panel of Figure 13 displays the photospheric velocity map obtained by the FLCT technique using *SOHO*/MDI magnetograms. The longest arrow corresponds to a velocity of 0.291 km $s^{-1}$. It may be noted from the flow map that the small, negative polarity spot shows clockwise shear flow motion whereas the positive polarity region (in which another footpoint was anchored of the lower loop system) shows counterclockwise flow motion. This linear translational motion evident in *TRACE* white light images, as well velocity shear flows as evident in FLCT images near the spots, most likely indicates the triggering of the shear in their locations. This physical mechanism most likely plays a role in the energy buildup of flares and generates the coalescence instability in the lower loop system.

### *2.4. Magnetic Topology of the Interacting Loop Systems*

In this section, we discuss the large-scale structure of a magnetic field responsible for the solar flare. The soft X-ray image of the flare clearly reveals that the two large solar loops (L1 and L2) cross each other and exhibit the X-type interaction. The chromospheric images (H$\alpha$ and *TRACE* 1600 Å) show the two-ribbon morphology with four kernels, i.e., four footpoints of the reconnected loops. We illustrate these features of the interacting loop systems in terms of the topological models (see Chapter 3 in Somov 2007). Figure 14 displays the field lines that connect the H$\alpha$ kernels: FP1 (L1) with FP2 (L1) and FP1 (L2) with FP2 (L2). The shaded regions FR1 and FR2 indicate the flare ribbons. They are located on both sides of the photospheric neutral line NL. Chromospheric evaporation along the reconnected field lines creates the SXR loops that look like they are crossing or touching each other somewhere near the top of a magnetic-field separator X. The loops and ribbon morphology shown in the observations qualitatively match this cartoon.

It is very likely that, in addition to what is shown in Figure 14, the electric currents and twisted magnetic fields can be created inside the interacting loops by some subphotospheric or photospheric mechanisms observed in the photosphere as shear motions or rotations. Such currents certainly must exist in complex active regions with sunspot rotation and large-scale photospheric shear flows. If the currents are mostly parallel, they attract each other and can give energy to a flare (Gold & Hoyle 1960). On the other hand, according to the simplified topological model presented in Figure 14, the flare energy comes from an interaction of magnetic fluxes that can be mostly potential. If this would be the case, the flare energy before a flare should mainly be stored in a slowly reconnecting current layer at the separator of coronal magnetic field. This possibility seems to be in agreement with the quadrupole reconnection model of solar flares. The morphology of the loops is also in agreement with the PFSS extrapolation of photospheric magnetic fields into the corona. Therefore, we consider both models intially from the view point of global magnetic configuration of a quadrupole-type active region taking into account the interacting electric currents.

Figure 15 illustrates the possible configuration of two large-scale coronal currents $J_1$ and $J_2$ distributed inside two different magnetic cells, i.e., the two magnetic fluxes of different linkages that interact and reconnect at the separator $X$. The two field lines $B_1$ and $B_2$ belong to the magnetic cells that connect the kernel FP2 (L2) with FP1 (L2) and the kernel FP2 (L1) with FP1 (L1), respectively. The coronal currents are distributed in some way inside the two different magnetic cells and the total currents $J_1$ and $J_2$ are shown schematically along the field lines $B_1$ and $B_2$.

If the field lines $B_1$ and $B_2$ near the current layer along the separator have opposite directional components, then they can be reconnected. If the two current systems $J_1$ and $J_2$ flow more or less in the same direction, then they also attract each other according to Gold & Hoyle (1960). The components of the magnetic field that are transverse to the separator reconnect; and they make the electric currents flowing along them also reconnect in the same way (Henoux & Somov 1987; Somov

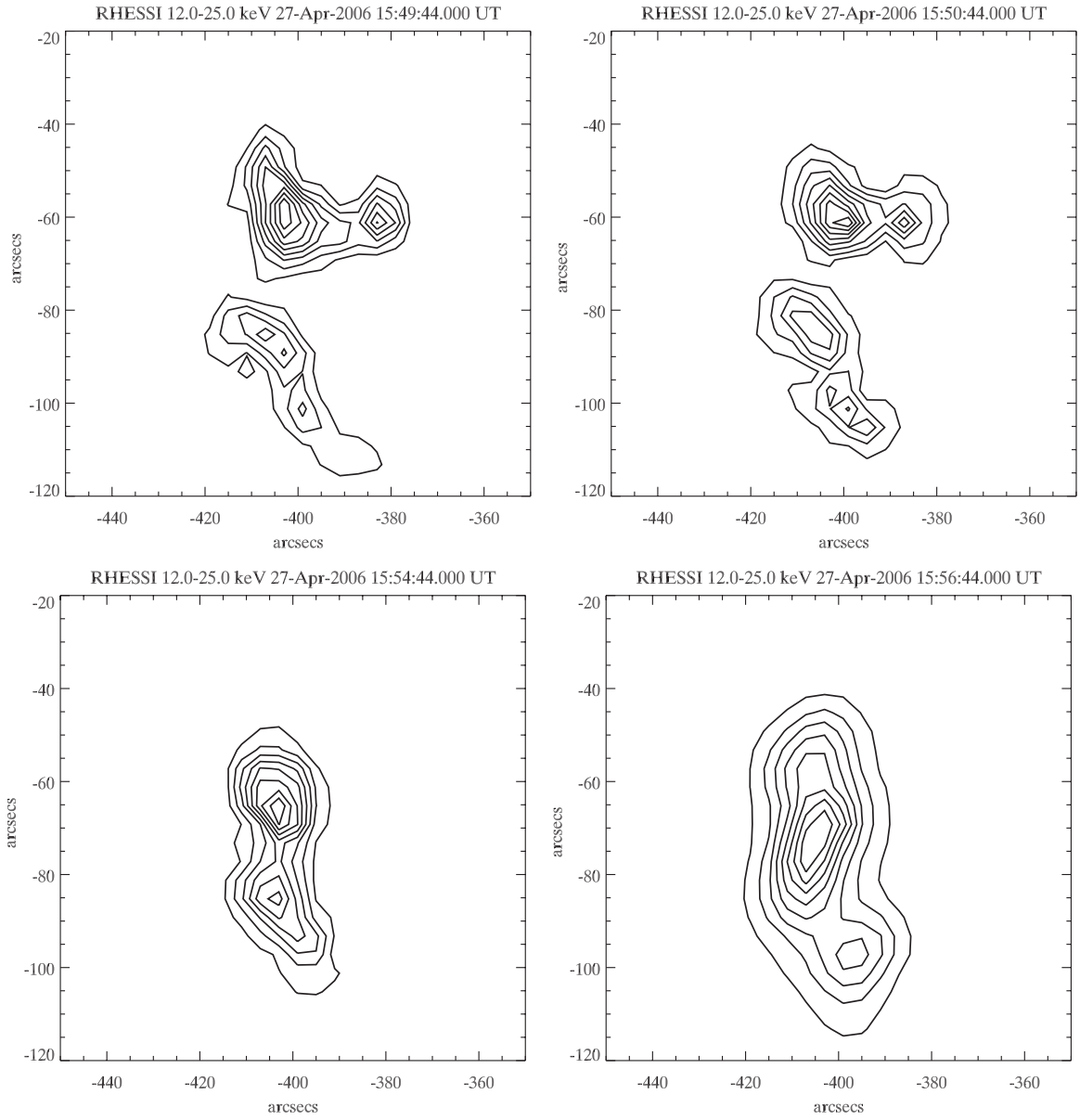


**Figure 9.** *RHESSI* images in the 12–25 keV energy bands reconstructed with the PIXON algorithm (contour levels for each image are 40%, 60%, 80%, and 95% of peak flux).

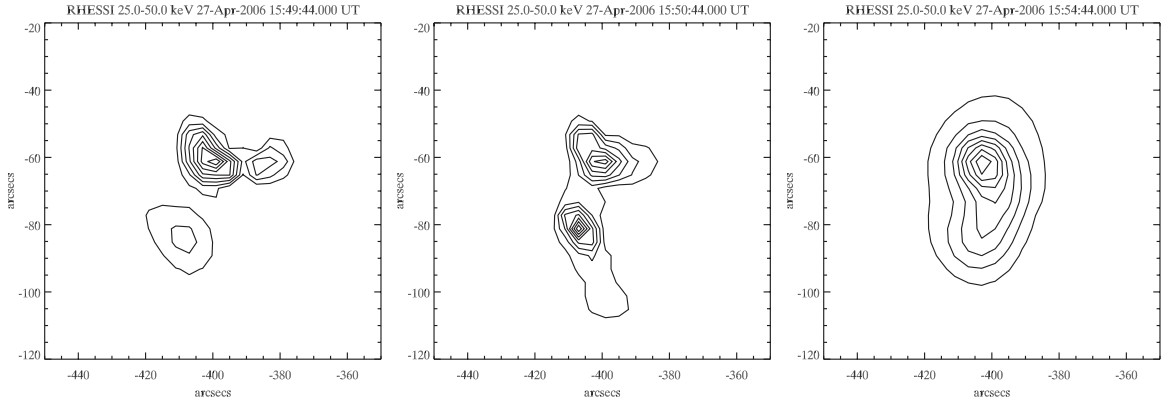


**Figure 10.** *RHESSI* images in 25–50 keV energy bands reconstructed with the PIXON algorithm (contour levels for each image are 40%, 60%, 80%, and 95% of peak flux).

1992). In this way, with a perpendicular magnetic field inside the place of interruption, magnetic reconnection can create local interruptions of the electric currents in the solar atmosphere. If these currents are highly concentrated, their interruption can give rise to strong electric fields that accelerate the energetic particles and can contribute significantly to the flare energetics.

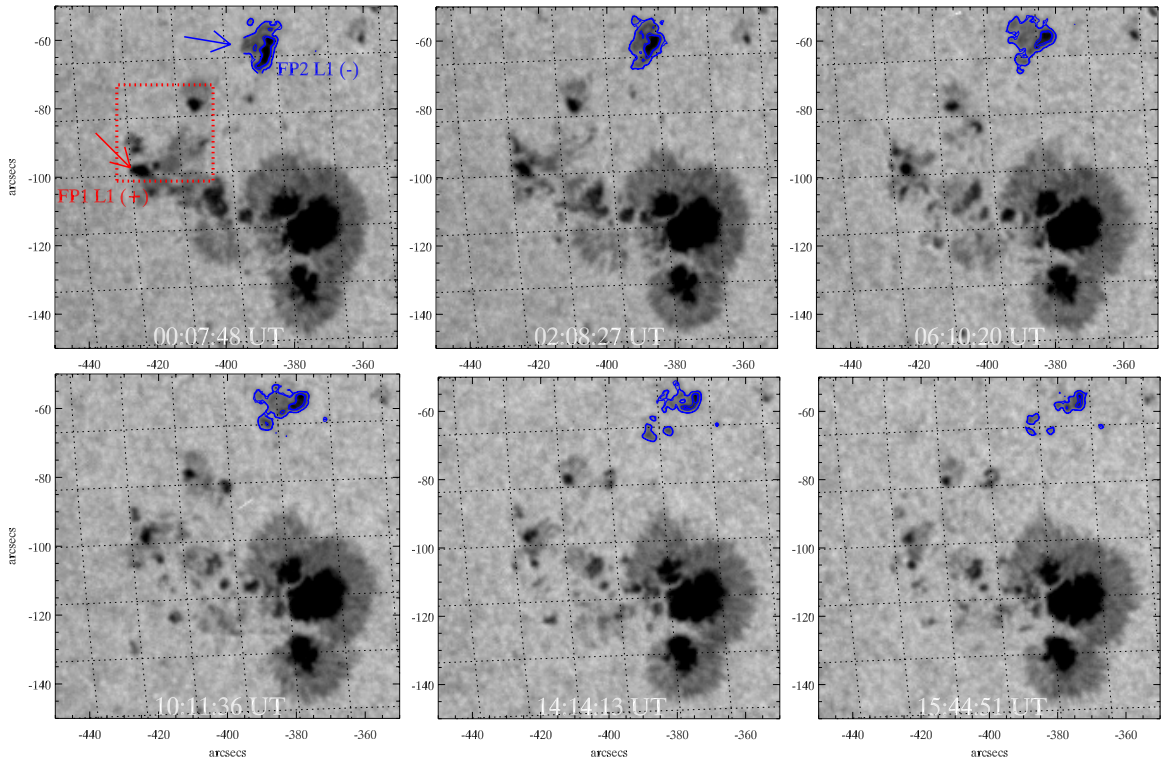


**Figure 11.** *TRACE* white-light images of the active region showing the linear/shear motion of negative polarity sunspot (indicated by blue contours). FP1 (red) and FP2 (blue) in the top left image show the "+ve" and "–ve" footpoints (indicated by arrows) of the lower loop system, respectively.
(A color version of this figure is available in the online journal.)

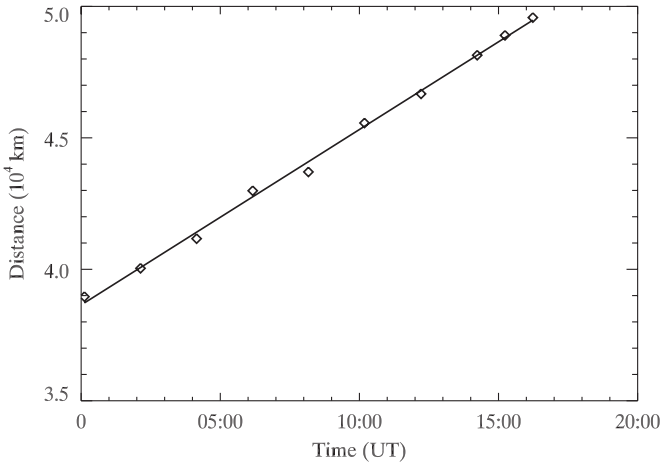


**Figure 12.** Linear motion of negative polarity sunspot on 2006 April 27. One footpoint of the loop system was anchored in this sunspot. The estimated speed of the sunspot from the linear fit is ~0.2 km $s^{-1}$ (662 km $h^{-1}$). This motion probably caused the destabilization and interaction in the loop systems.

What factors determine the rate of magnetic reconnection in the current layer at the separator? Let us consider the magnetic fields created by the currents $J_1$ and $J_2$. These additional or secondary fields play the role of the longitudinal magnetic field near the reconnecting current layer. Being superimposed on the large-scale potential field, they create two types of field line spirals, i.e., left handed and right handed. When looking along the positive direction of the field lines $B_1$ and $B_2$, we see the two opposite orientations for the spirals to the right for the dextral structure and to the left for the sinistral one. Depending on this handedness property, known as chirality, and also depending on the angle between the currents $J_1$ and $J_2$, magnetic reconnection of electric currents will proceed faster or slower (Henoux & Somov 1987).

As evident in the observations as well as in the theoretical baseline, the X-type reconnection may produce the plasma jets. However, we have no observational signature of such jets in our observations. In the flare under consideration, the reconnected fast outflows from a current layer relax quickly because they interact with (1) closed field lines of quadrupole type of the active region (recall that there was no type III radioburst; thus the opening of field lines did not take place during the flare energy release); and/or (2) chromospheric evaporation upflows (the energy released in closed magnetic configuration goes into impulsive heating of the upper chromosphere to high temperatures, which is why the soft X-ray images become so bright quickly).

## 3. SOME THEORETICAL ESTIMATIONS

The *RHESSI* temporal images (12–25 and 25–50 keV) reveal the coalescence of the loop-top sources of the interacting loop system. The two loop-top sources merge approximately vertically in the *RHESSI* field of view. Therefore, the lower bound change in the distance of the two approaching loops is

$$\Delta l_{\rm coal} \approx 22{,}000 \text{ km} \quad (1)$$

and the elapsing time is

$$\Delta \tau_{\rm coal} \approx 420 \text{ s}. \quad (2)$$

The coalescence instability may be activated in the observed interacting loop system, which is the effect that merges the two isolated magnetic islands into a single one (Haruki & Sakai 2001a, 2001b; Aschwanden 2004). This type of instability

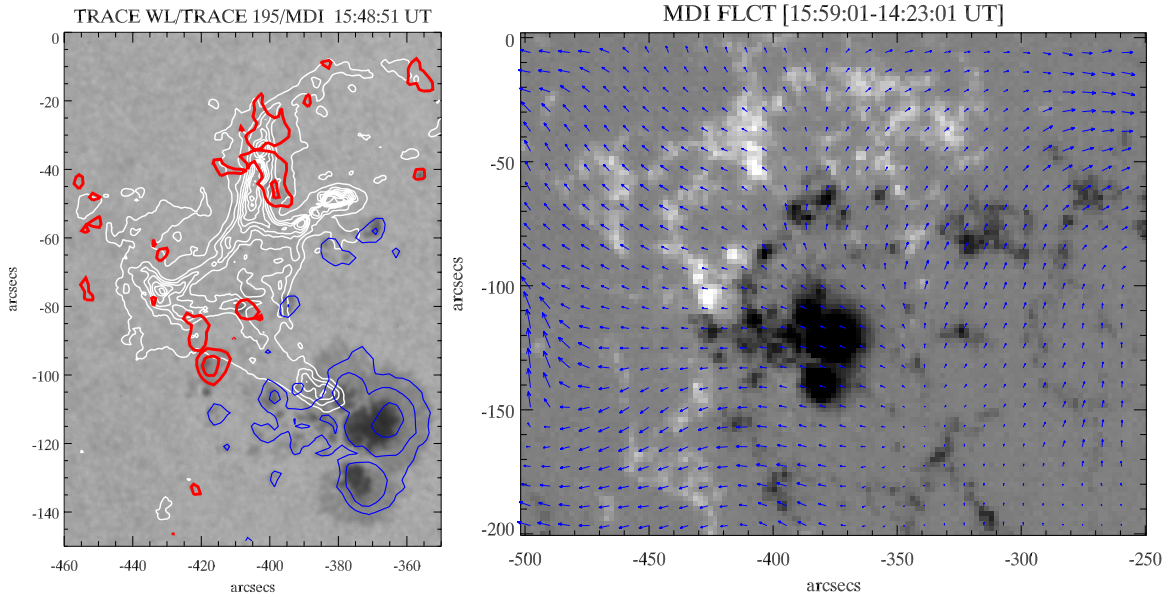


**Figure 13.** Left: *TRACE* 195 Å (white) and MDI magnetogram contours overlaid on the *TRACE* white-light image. Red contours indicate the positive polarity sunspots whereas the blue ones show the negative polarity spots. The contour levels are ±500, ±1000, ±2000, ±3000 G. Right: the photospheric velocity map obtained from the Fourier Local Correlation Tracking (FLCT) technique using *SOHO*/MDI magnetograms. The longest arrow corresponds to the velocity of 0.291 km $s^{-1}$.

(A color version of this figure is available in the online journal.)

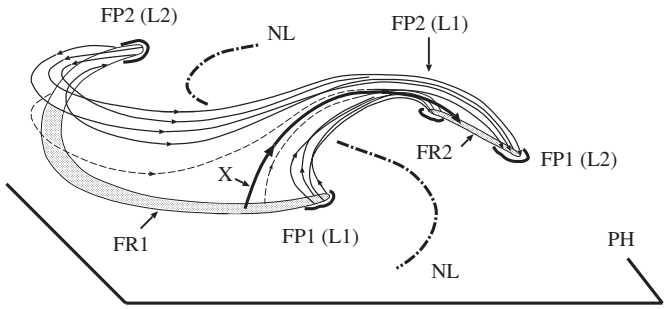


**Figure 14.** Magnetic field lines that connect the H$\alpha$ kernels FP1 (L1), FP2 (L1), FP1 (L2), and FP2 (L2) are passing through a region of primary energy release located somewhere near the top of the separator X. The flare ribbons FR1 and FR2 are formed where these field lines cross the photospheric plane PH. NL is the neutral line of the photospheric magnetic field. Chromospheric evaporation creates a picture of the crossing soft X-ray loops.

evolves in two phases: the first phase involves the pairing of the current filament/loops as in the ideal MHD process, while the second phase is the resistive phase of pairwise reconnection between the approaching current-carrying flux tubes. The numerical MHD simulations reveal the different phases of coalescence instability in ideal/resistive solar plasma (Schumacher & Kliem 1997).

The characteristic timescale of the ideal phase of coalescence instability is a multiple of the Alfvénic transit time (Aschwanden 2004):

$$\tau_{\rm coal} = \frac{1}{q_{\rm coal}} . \frac{l_{\rm coal}}{v_A}, \tag{3}$$

where

$$q_{\rm coal} = \frac{u_{\rm coal}}{v_A}. \tag{4}$$

$l_{\rm coal}$, $u_{\rm coal}$ and $v_A$ are, respectively, the distance between approaching loops, approaching velocity, and the local Alfvénic speed. Using Equations (3) and (4), the differential coalescence speed is

$$\Delta u_{\rm coal} = \frac{\Delta l_{\rm coal}}{\Delta \tau_{\rm coal}}. \tag{5}$$

Therefore, using the observationally estimated values as mentioned in Equations (1) and (2), we obtain an average coalescence speed of ∼52 km $s^{-1}$. *TRACE* 195 Å images also show the interacting and paired loops. Using these images, the projected distance–time profile of the interaction region (i.e., converging motion at the interaction site) is presented in Figure 4. The average converging speed of the interaction region is estimated as ∼30 km $s^{-1}$. The approximate approaching velocity of one magnetic island of a loop is evident as ∼26 km $s^{-1}$. The closeness in value of these two speeds is in agreement with loop coalescence.

By assuming that the typical Alfvénic speed at the interaction region is ∼1000 km $s^{-1}$ and the projected distance between the approaching loops $\Delta l_{\rm coal} \approx 22{,}000$ km, the estimated Alfvénic transit time of the region will be ∼22 s. Therefore, coalescence will occur $\sim 20\tau_A$ for our observation, which is rather longer than predicted in various simulation results by Sakai & de Jager (1996) and Tajima et al. (1982) under various assumptions of the model atmosphere. However, for $L \sim 62{,}800$ km, $\tau_A = 16$ s, the Reynolds number $(S = R) = 500$, $n_e = 10^{10}$ $cm^{-3}$, and $B_Z =$ 90 G, Milano et al. (1999) have found that two loops coalesce at $t = 11\tau_A$, with the magnetic energy and even its dissipation enhanced. The loop coalescence time depends upon various atmospheric parameters, and therefore further simulations will be interesting to study the dynamics and energetics of our observed coalesced loops.

We can estimate the amount of energy ($\mathcal{E}_c$) available due to coalescence instability (Tajima et al. 1982; Smartt et al. 1993) by

$$\mathcal{E}_c \approx \frac{LB^2a^2}{2} \ln \frac{L}{a}, \tag{6}$$

where $L$, $B$, and $a$ are the length of the reconnecting region, loop magnetic field, and the radius of the current loop, respectively.

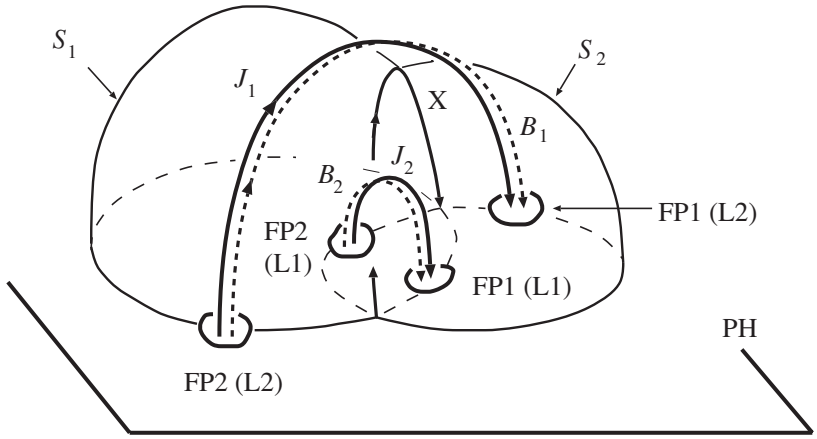


**Figure 15.** Three-dimensional model of the coronal magnetic field with two interacting electric currents $J_1$ and $J_2$. Four magnetic fluxes of different linkages are separated by the separatrices $S_1$ and $S_2$ that cross at the separator X above the photospheric plane PH. The two field lines $B_1$ and $B_2$ connect the kernel FP2 (L2) with FP1 (L2) and the kernel FP2 (L1) with FP1 (L1). The coronal currents are distributed somehow inside the two magnetic cells and are shown schematically as the total currents $J_1$ and $J_2$ along the field lines $B_1$ and $B_2$.

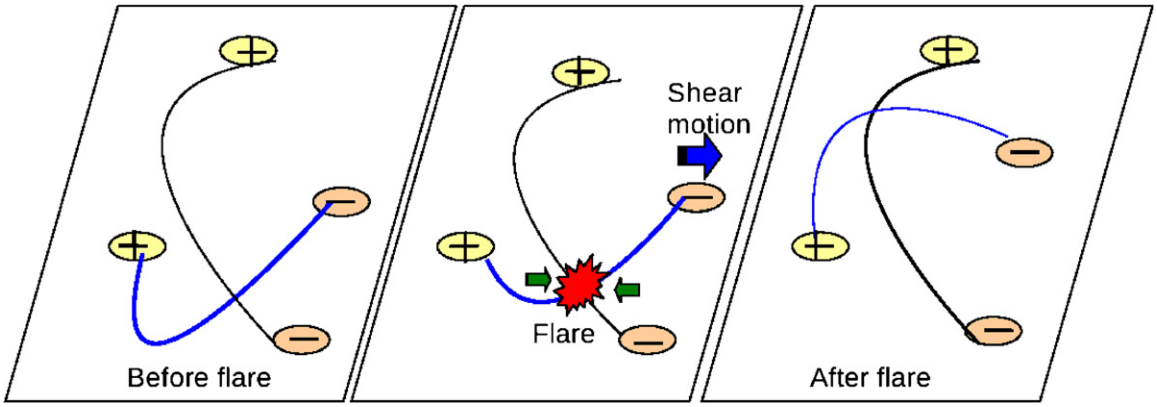


**Figure 16.** Schematic cartoons showing the flare triggering due to the interaction of two X-ray loop systems. The black line shows the higher-loop system and the dark blue line indicates the smaller underlying loop system. Due to the shear motion of the right footpoint of the smaller loop system, it becomes unstable and reconnects the overlying higher loop system, triggering a flare event. After the flare event, the lower loop system becomes simplified as evident in the *GOES* SXI image at 16:31:01 UT (Figure 2).

(A color version of this figure is available in the online journal.)

We take $B = 100$ G, $L = 22{,}000$ km, and $a = 11{,}000$ km, which gives

$$\mathcal{E}_c \approx 1.0 \times 10^{31} \text{ erg}. \quad (7)$$

Therefore, this value is comparable with the energy released during the M-class flare.

In general, the total magnetic field energy of the currents generated by photospheric vortex flows, sunspot rotation, or shear flows in the photosphere can exceed the energy of even the largest flares. However, in contrast to the thin current layer at the separator, these currents are typically dispersed over a large volume of magnetic flux tubes in the corona. The dissipation rate of the currents so distributed in the coronal plasma of very high conductivity is vanishingly small. However, their interaction with each other and with the current layers at the separator is not small and must be treated within the framework of the global electrodynamical coupling of a flare active region or a complex.

As described in Section 2.4, a distinctive feature of this interaction is that the separator is orthogonal (in the sense of magnetic field topology) to both systems of electric currents $J_1$ and $J_2$. For this reason, not only the magnetic field components associated with the current layer but also the longitudinal (guiding) components with respect to the separator are reconnected. Therefore, not only the energy associated with the current layer at the separator but also a part of the energy of the currents generated by the photospheric vortex flows, sunspot rotation, and shear flows is released in the flares (Henoux & Somov 1987; see also Somov et al. 2002).

All of the above are concerned with the large-scale structure of magnetic fields and electric currents in large solar flares whose main features can be qualitatively described by simplified topological models. However, in actual flares there are many different structures of different scales including very small ones. In the flare under consideration, we see many interacting small flux threads/tubes (e.g., Figure 3). Moreover, the image at 15:48 UT in this figure shows the loop–loop interaction and formation of the "X" point in between the interacting loop system. So, it is likely that the observed flare was caused by interactions of not only two but a multitude of loops forming more or less parallel systems that are visible in low-resolution images as single wide loops. From a theoretical point of view, this presumably means that the distributed currents $J_1$ and $J_2$ are deeply pinched in many thin current filaments. Therefore, what we observe is some average picture of reconnection with some average reconnection rate.

## 4. DISCUSSION AND CONCLUSIONS

We present rare observational evidence of X-type loop–loop interaction associated with the M7.9/1N flare. The coronal images obtained by *GOES* SXI and *TRACE* 195 Å clearly show the interacting loop system. *TRACE* white-light images reveal the shear motion of the sunspots (negative polarity) across the neutral line. This shear motion probably might have produced the destabilization in the associated loop system and caused the loop interaction followed by the flare. Based on multiwavelength observations, we draw a schematic cartoon to explain the whole event (see Figure 16). Before the flare there were two loop systems visible in the SXI images, a higher loop in the N–S direction and another smaller loop system in the E–W direction lying below this higher loop system. Due to the shear motion of the right footpoint (anchored in negative polarity) of the smaller loop system, the loop becomes unstable and rises up due to instability and reconnects the overlying higher loop system, resulting in X-type interaction associated with the flare event. After the flare event, the connectivity of the smaller loop system changed into the relaxed state.

The regular variation of the 4.9 and 8.8 GHz radio fluxes and accompanying flare effect observed during 2006 April 27 are interpreted using the X-type loop interaction model. We found that the double-peak structure exhibited oscillatory behavior. Double peak in the radio flux gives support for the loop-interaction model (Sakai et al. 1986). According to the theoretical model, the double-peak structure is more pronounced when the currents in the two loops are sufficient for explosive coalescence. The individual peak belongs to the electric field variation at the reconnection site. This electric field accelerates the electrons that generate the radio emission. The cause of quasiperiodic oscillation is as follows: after explosive reconnection poloidal magnetic fields take place at the "X" point between the approaching current loop, the two plasma blobs pass through each other and overshoot (an approach that fails and gives way to another attempt), resulting in the repetition of the process. Kliem et al. (2000) also proposed a model in which the pulsations of the radio flux are caused by quasi-periodic particle acceleration episodes that result from a dynamic phase of magnetic reconnection in a large-scale current sheet. The reconnection is dominated by repeated formation and subsequent coalescence of magnetic islands, while a continuously growing plasmoid is fed by newly coalescing islands. In our case, the coalescence speed of 52 km $s^{-1}$ is much smaller than the Alfvén velocity of $\sim$1000 km $s^{-1}$. In the preflare stage, multiple current filament structures might be generated due to the photospheric shear motion across the neutral line. The photospheric shear motion can give rise to plasma currents along the potential magnetic field produced by the sunspots close to the active region. As the shear motion proceeds, the current density may increase and the current loop might move upward; this is associated with the relaxation of magnetic tension (Sakai et al. 1986). The absence of type III bursts during flare energy release confirms the connectivity change and no opening of field lines. In addition, coalescence of hard X-ray sources also confirms the loop–loop interaction.

Sakai et al. (1986) presented the physical characteristics of the explosive coalescence of current loops through computer simulation and theory and defined the canonical characteristics of explosive coalescence as (1) impulsive increase of kinetic energy of electrons and ions, (2) simultaneous heating and acceleration of particles in high- and low-energy spectra (i.e., Neupert effect), (3) quasi-periodic amplitude oscillations in field and particle quantities, and (4) a double-peak (or triple peak) structure in these profiles. Our observations clearly match with all the above-mentioned characteristics of explosive coalescence and provide unique evidence of X-type loop–loop interaction satisfying theories and simulations.

The interaction of large-scale current-carrying loops should be considered as part of the global electrodynamic coupling in flare-producting active regions and active complexes as discussed in Section 2.4. On the one hand, the potential magnetic field in the corona determines the large-scale structure of active regions while the reconnecting current layers at separators in the corona, together with other non-potential components (see Section 14.5 in Somov 2007) of the magnetic field, determine the energetics and dynamics of large flares. On the other hand, two large-scale current-carrying loops emerging from under the photosphere also have sufficient energy to produce a large flare by their interaction and coalescent instability as considered in this paper. Moreover, these two currents could be incorporated in the large-scale structure through the reconnecting current layer.

The principal question is in the relative role of two distinct sources of free magnetic energy: the interaction of magnetic fluxes and the interaction of electric currents as demonstrated in this paper. Clearly, the answer depends on the relation between (1) the photospheric flows that create the preflare current layers at the separators, (2) the photospheric shear flows that induce the current layers extending along the separatrices (Somov et al. 2002), and (3) the other photospheric flows such as sunspot rotations which twist the magnetic flux tubes. In any case, the separator is a special place where a fast conversion of free magnetic energy into bulk plasma motions, heat flows, and energy of accelerated particles can take place.

In conclusion, we found a rare multiwavelength observational signature of loop–loop interaction that triggered an M-class flare, which is consistent with the earlier developed theories and simulations. However, further detailed multiwavelength studies should be carried out statistically by analyzing such events to shed more light on the dynamics and energetics related to the flare and eruptive phenomena related to loop–loop interactions.

We express our gratitude to the referee for valuable suggestions which improved the manuscript considerably. We acknowledge the space missions *GOES*, *SOHO*/MDI, *TRACE,* and *RHESSI* for providing the data used in this study. *Solar and Heliospheric Observatory* (*SOHO*) is a project of international cooperation between ESA and NASA. We are thankful for the radio data obtained from the RSTN network (Sagamore Hill) and the radiospectrograph from Ondrejov, Czech Republic. We are thankful for the Meudon H$\alpha$ data used in this study. The Global High Resolution H$\alpha$ Network is operated by the Space Weather Research Lab, New Jersey Institute of Technology. A.K.S. thanks SP2RC, Department of Applied Mathematics, The University of Sheffield, for supporting the collaborative visit where part of the present research work was carried out. A.K.S. also acknowledges the joint DST-RFBR (INT/RFBR/P-38) project grant for the financial support of this work. B.V.S. thanks the Russian Foundation for Fundamental Research (grant No. 08-02-01033). R.E. acknowledges M. Kéray for patient encouragement and is also grateful to NSF, Hungary (OTKA, Ref. No. K67746) for financial support received. We also thank Dr. Marc DeRosa for his valuable suggestions and discussions regarding the use of the PFSS technique. We thank the editors of

the journal for correcting the English language which improved the clarity of the paper.

## REFERENCES


Altschuler, M. D., & Newkirk, G. 1969, Sol. Phys., 9, 131
Aschwanden, M. J. 2004, Physics of the Solar Corona: An Introduction (Chichester: Praxis)
Falewicz, R., & Rudawy, P. 1999, A&A, 344, 981
Fisher, G. H., & Welsch, B. T. 2008, in ASP Conf. Ser. 383, Subsurface and Atmospheric Influences on Solar Activity, ed. R. Howe et al. (San Francisco, CA: ASP), 373
Gold, T., & Hoyle, F. 1960, MNRAS, 120, 89
Gorbachev, V. S., & Somov, B. V. 1989, SvA, 33, 57
Gorbachev, V. S., & Somov, B. V. 1990, Adv. Space Res., 10, 105
Hanaoka, Y. 1996, Sol. Phys., 165, 275
Handy, B. N., et al. 1999, Sol. Phys., 187, 229
Haruki, T., & Sakai, J. 2001a, APJ, 552, L175
Haruki, T., & Sakai, J. I. 2001b, Phys. Plasmas, 8, 1538
Henoux, J. C., & Somov, B. V. 1987, A&A, 185, 306
Hill, S. M., et al. 2005, Sol. Phys., 226, 255
Jiricka, K., Karlicky, M., Kepka, O., & Tlamicha, A. 1993, Sol. Phys., 147, 203
Jiřička, K., & Karlický, M. 2008, Sol. Phys., 253, 95
Karlický, M., & Jiřička, K. 2003, in Solar Variability as an Input to the Earth's Environment, ed. A. Wilson (ESA-SP 535; Noordwijk: ESA), 499
Kliem, B., Karlický, M., & Benz, A. O. 2000, A&A, 360, 715
Kumar, P., Manoharan, P. K., & Uddin, W. 2010, ApJ, 710, 1195
Kumar, P., Srivastava, A. K., Filippov, B., & Uddin, W. 2010, Sol. Phys., 266, 39
Liu, R., Gilbert, H. R., Alexander, D., & Su, Y. 2008, ApJ, 680, 1508
Liu, Y., Akioka, M., Yan, Y., & Sato, J. 1998, Sol. Phys., 180, 377
Milano, L. J., Dmitruk, P., Mandrini, C. H., Gómez, D. O., & Démoulin, P. 1999, ApJ, 521, 889
Neupert, W. M. 1968, ApJ, 153, L59
Pizzo, V. J., et al. 2005, Sol. Phys., 226, 283
Pohjolainen, S. 2003, Sol. Phys., 213, 319
Sakai, J., & de Jager, C. 1989, Sol. Phys., 123, 389
Sakai, J., & de Jager, C. 1996, Space Sci. Rev., 77, 1
Sakai, J., Nakajima, H., Zaidman, E., Tajima, T., Kosugi, T., & Brunel, F. 1986, in NASA Conference Publication, Vol. 2449, ed. B. R. Dennis, L. E. Orwig, & A. L. Kiplinger (Greenbelt, MD: NASA Goddard Space Flight Center), 393
Schatten, K. H., Wilcox, J. M., & Ness, N. F. 1969, Sol. Phys., 6, 442
Schumacher, J., & Kliem, B. 1997, Adv. Space Res., 19, 1797
Smartt, R. N., Zhang, Z., & Smutko, M. F. 1993, Sol. Phys., 148, 139
Somov, B. V. 1992, Physical Processes in Solar Flares (Dordrecht: Kluwer)
Somov, B. V. 2007, Plasma Astrophysics, Part II: Reconnection and Flares (New York: Springer)
Somov, B. V., Kosugi, T., Hudson, H. S., Sakao, T., & Masuda, S. 2002, ApJ, 579, 863
Srivastava, A. K., Zaqarashvili, T. V., Kumar, P., & Khodachenko, M. L. 2010, ApJ, 715, 292
Tajima, T., Brunel, F., & Sakai, J. 1982, ApJ, 258, L45
Tan, C., Chen, P. F., Abramenko, V., & Wang, H. 2009, ApJ, 690, 1820
Tsuneta, S., Masuda, S., Kosugi, T., & Sato, J. 1997, ApJ, 478, 787
Yokoyama, T., Akita, K., Morimoto, T., Inoue, K., & Newmark, J. 2001, ApJ, 546, L69